Multiscale model of global inner-core anisotropy induced by hcp alloy plasticity

A. Lincot, Ph. Cardin, R. Deguen, S. Merkel

Multiscale model of global inner-core anisotropy induced by hcp alloy plasticity

A. Lincot[1,2], Ph. Cardin[1], R. Deguen[3], and S. Merkel[2,4]

[1]ISTerre, Université Grenoble Alpes, CNRS, Grenoble, France, [2]UMET, Unité Matériaux et Transformations, CNRS, INRA, ENSCL, Université de Lille, Lille, France, [3]Laboratoire de géologie de Lyon, ENS de Lyon, Université Lyon-1, Lyon, France, [4]Institut Universitaire de France, Paris, France

Abstract The Earth's solid inner core exhibits a global seismic anisotropy of several percents. It results from a coherent alignment of anisotropic Fe alloy crystals through the inner-core history that can be sampled by present-day seismic observations. By combining self-consistent polycrystal plasticity, inner-core formation models, Monte-Carlo search for elastic moduli, and simulations of seismic measurements, we introduce a multiscale model that can reproduce a global seismic anisotropy of several percents aligned with the Earth's rotation axis. Conditions for a successful model are an hexagonal close packed structure for the inner-core Fe alloy, plastic deformation by pyramidal $\langle c + a \rangle$ slip, and large-scale flow induced by a low-degree inner-core formation model. For global anisotropies ranging between 1 and 3%, the elastic anisotropy in the single crystal ranges from 5 to 20% with larger velocities along the c axis.

1. Introduction

Seismic observations using body waves differential travel times [*Poupinet et al.*, 1983; *Morelli et al.*, 1986; *Waszek et al.*, 2011], long period normal modes [*Woodhouse et al.*, 1986; *Deuss et al.*, 2010], and the analysis of autocorrelation of earthquake coda [*Wang et al.*, 2015] provide strong evidences that the Earth's inner core is anisotropic, with P waves traveling faster by up to 3% in the polar than in the equatorial direction. Further analyses refined this observation, providing evidences for both hemispherical and radial variations of the amplitude of anisotropy [*Tkalčić*, 2015; *Deuss*, 2014; *Wang et al.*, 2015]. However, this apparent complexity should not obscure the first-order observation that the fast propagation direction for inner-core seismic waves is aligned with the Earth's rotation axis. The observed axial anisotropy still lacks a conclusive explanation. This paper will hence focus on reproducing this first-order observation from a multiscale model.

A multiscale model of inner-core anisotropy should allow to build a synthetic inner core with a given choice of crystal structure, elastic moduli, and crystal alignment mechanism, coupled with an inner-core formation hypothesis. In a second stage, the model should simulate present-day seismic observations which can then be compared with actual measurements (Figure 1) [*Lincot et al.*, 2014].

In this work, we investigate whether such integrated model can indeed reproduce the first-order observation of several percents North-South global seismic anisotropy in the inner core. The abundance of symmetries for elasticity and plasticity of body-centered cubic (bcc) and face-centered cubic (fcc) phases combined with the integrated nature of inner-core anisotropy measurements is such that plastic deformation of such crystal structures cannot explain the global inner-core anisotropy [*Lincot et al.*, 2015]. Here we investigate the effect of an hexagonal close packed (hcp) structure for the inner-core Fe alloy. Under the assumption that the inner-core anisotropy results from plastic deformation along a dominant slip system, we find that necessary conditions for a successful anisotropic model are 5 to 20% single-crystal elastic anisotropy, plastic deformation by pyramidal slip, and a large-scale flow induced by a low-degree inner-core formation model.

2. Methods
2.1. Inner-Core Formation Model
It is typically assumed that the inner-core anisotropic structure results from an alignment of anisotropic Fe alloy crystals acquired either during solidification [*Bergman*, 1997; *Deuss et al.*, 2010] or as a result of subsequent deformation [*Yoshida et al.*, 1996; *Karato*, 1999; *Wenk et al.*, 2000a; *Deguen*, 2012] although other models
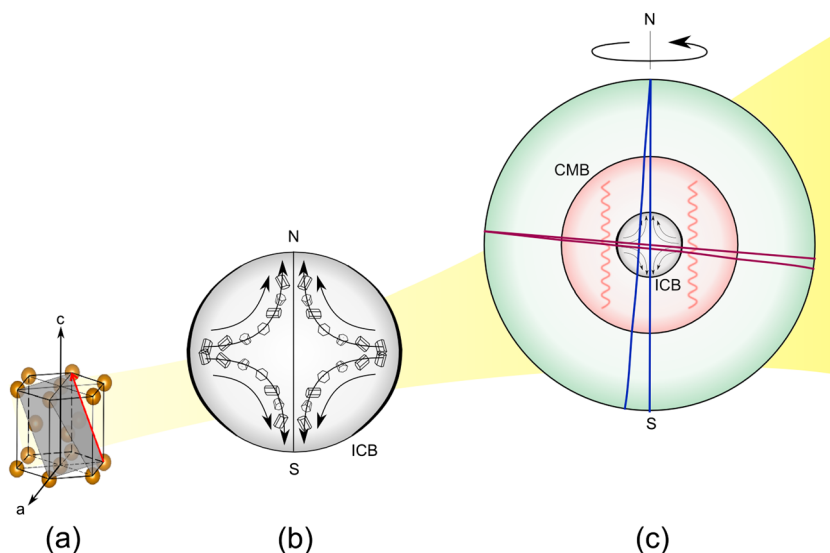
Figure 1. Multiscale model of inner-core anisotropy. (a) Anisotropic hexagonal Fe alloy crystals plastically rotate through slip under (b) the action of deformation in the inner core. (c) Deformation in the inner core depends on the core formation model, driven by heat extracted by outer core convection. At the global scale, seismic anisotropy is measured with body-wave differential travel times (Figure 1c) which are faster along the North-South axis (blue trajectories) than in the equatorial plane (red trajectories).

have been proposed assuming, for instance, the presence of aligned aspherical liquid inclusions in the inner core [*Singh et al.*, 2000].

Radial dendritic growth [*Bergman*, 1997] aligns the crystals relative to the spherical inner-core boundary (ICB) which is unlikely to produce a global cylindrical axisymmetric anisotropy [*Lincot et al.*, 2014]. An additional orientation mechanism is required for aligning the fast *P* wave crystal directions with the Earth's rotation axis. Two classes of processes have been suggested in the literature: (i) a forcing of inner-core dynamics from the outer core magnetic field [*Karato*, 1999; *Buffett and Wenk*, 2001] and (ii) an effect of the Earth's rotation through the ellipticity of a convective inner core [*Buffett*, 2009] or inner-core preferential growth [*Yoshida et al.*, 1996]. Recent studies evaluated that the direct effect of the Lorentz forcing generates weak deformation [*Lasbleis et al.*, 2015]. The effect of the magnetic field on anisotropy would result from solidification textures mostly, which are not well understood at inner-core conditions and have not been observed in analog experiments [*Brito et al.*, 2002]. In addition, recent calculations of the thermal conductivity of Fe at core conditions [*Zhang et al.*, 2015] indicate that thermal convection is unlikely in the inner core [*Deguen*, 2012], although compositional convection may be an option [*Gubbins et al.*, 2013].

We therefore focus on models of inner-core growth with faster solidification in the equatorial plane (Figure 2a) [*Yoshida et al.*, 1996], with solidification texturing (Figure 2b) [*Bergman*, 1997] and/or density stratification (Figure 2c) [*Deguen and Cardin*, 2009] as possible additional ingredients. In all cases, we impose a solidification rate twice as large at the equator than at the poles. Figure 2a assumes random solidification textures while Figure 2b includes solidification textures in which the *c* axes of the hcp crystals lie preferentially in the plane of the ICB. Figure 2c accounts for a stable density stratification during inner-core formation. The importance of stratification depends on the value of the buoyancy number $\mathcal{B}^* = \frac{\Delta\rho\, g\, r_{ic}^2}{\eta\, \dot{r}_{ic}}$, where $\Delta\rho$ is the density difference across the inner core associated with compositional or thermal stratification (excluding the contribution of compression), g the acceleration of gravity at the ICB, η the dynamic viscosity of the inner core, r_{ic} the inner core radius, and $\dot{r}_{ic}$ the inner core growth rate [*Deguen and Cardin*, 2009]. Density stratification tends to localize the deformation in a thin shear layer below the ICB, whose thickness decreases with increasing $|\mathcal{B}|$, and in which the strain rate increases with $|\mathcal{B}|$. In this study, we set $\mathcal{B}^* = -10^6$ (corresponding to $\Delta\rho \simeq 5$ kg m^{-3} and $\eta \simeq 10^{18}$ Pa s). Larger $\mathcal{B}^*$ values would result in earlier stratification in the Earth's history and, consequently, reduce the central part of pure shear deformation [*Deguen and Cardin*, 2009; *Deguen et al.*, 2011]. Also note that Figure 2c assumes random solidification textures at the ICB. Deformation is large in such model, and hence, solidification textures are quickly erased and do not play an important role in the modeled global
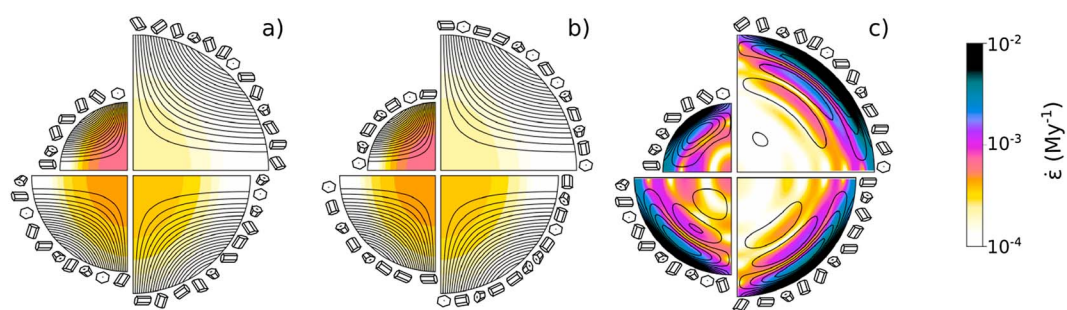
Figure 2. Inner-core formation models with preferential growth of the inner core at the equator [*Yoshida et al.*, 1996]. The resulting topography is continuously relaxed by a quadrupolar flow, generating plastic deformation of the inner core Fe alloy. (a) Random crystallization textures at the ICB while (b) solidification textures in which the *c* axes of the hcp crystals lie preferentially in the plane of the ICB. (c) A stable density stratification during inner-core formation. Each figure shows the time evolution of flow during the inner-core history at nondimensional times $t = 0.25, 0.5, 0.75$, and 1, where 0 is the formation of the inner core and 1 is the present day, starting anticlockwise from the upper left quadrant. Colors are Von-mises equivalent strain rate $\dot{\epsilon}$ (in Myr^{-1}, log scale). Black lines in overlay are representative streamlines.

scale anisotropy, as in this study, but can play a crucial role for studies focused on the superficial layer of the inner core.

As illustrated in Figure 2, a model reproducing present-day seismic observations should integrate the whole history of the inner core. In that view, seismic anisotropy is a marker of inner-core formation and evolution and will record changes in dynamics or mineralogy during its history.

2.2. Inner-Core Fe Alloy Textures

For each inner-core formation model, we assume plastic deformation of the inner-core Fe alloy on a dominant slip system. We follow the deformation of 100 markers introduced at the ICB during inner-core growth and calculate the corresponding textures for a 10,000 grains aggregate using the visco-plastic self-consistent code of *Lebensohn and Tomé* [1993]. Experiments on Fe and analogs indicate that basal slip and twinning dominate the plastic behavior of hcp Fe at low temperature [*Wenk et al.*, 2000b; *Merkel et al.*, 2004] and that as temperature increases, twinning disappears and the activity of pyramidal $\langle c + a \rangle$ slip increases [*Poirier and Langenhorst*, 2002; *Miyagi et al.*, 2008; *Merkel et al.*, 2012]. We simulate the texture of an hcp aggregate at each marker for three different dominant slip systems: basal, prismatic, and pyramidal $\langle c + a \rangle$ (Table 1). The final results are meridional maps of textures for a present-day inner core (Figure 3).

This results in a striking observation: simulations with the pyramidal $\langle c + a \rangle$ slip system are very efficient at aligning the *c* axes of the polycrystals with the Earth's rotation axis. Simulations with other slip systems can induce strong textures at the local scale but, over the scale of the inner core, the hcp alloy alignment is not consistent. Indeed, unlike basal and prismatic slip, pyramidal $\langle c + a \rangle$ slip includes *c* in the slip direction: it is prone to align the *c* axes of the aggregate during deformation.

Table 1. Normalized Critical Resolved Shear Stresses Used for Calculating the Development of Texture in the hcp Aggregate for Models With the Following Dominant Slip Systems: Basal, Prismatic, Pyramidal $\langle c + a \rangle$ First Order, Pyramidal $\langle c + a \rangle$ Second Order[a]

Slip System		Dominant Slip System			
		Basal	Prismatic	Pyr. $\langle c + a \rangle$ 1	Pyr. $\langle c + a \rangle$ 2
Basal	$(0001) \langle 11\bar{2}0 \rangle$	0.5	1.0	2.0	2.0
Prismatic	$\{1\bar{1}00\} \langle 11\bar{2}0 \rangle$	1.0	0.5	2.0	2.0
Pyr. $\langle a \rangle$	$\{1\bar{1}01\} \langle 11\bar{2}0 \rangle$	3.0	3.0	3.0	3.0
Pyr. $\langle c + a \rangle$ 1st order	$\{\bar{1}011\} \langle 11\bar{2}3 \rangle$	2.0	2.0	0.5	∞
Pyr. $\langle c + a \rangle$ 2nd order	$\{\bar{1}122\} \langle 11\bar{2}3 \rangle$	∞	∞	∞	0.5

[a]The pyramidal $\langle a \rangle$ slip system is weakly activated in all cases. Results for simulations using both pyramidal $\langle c+a \rangle$ slip systems are nearly identical and are presented together in the paper.
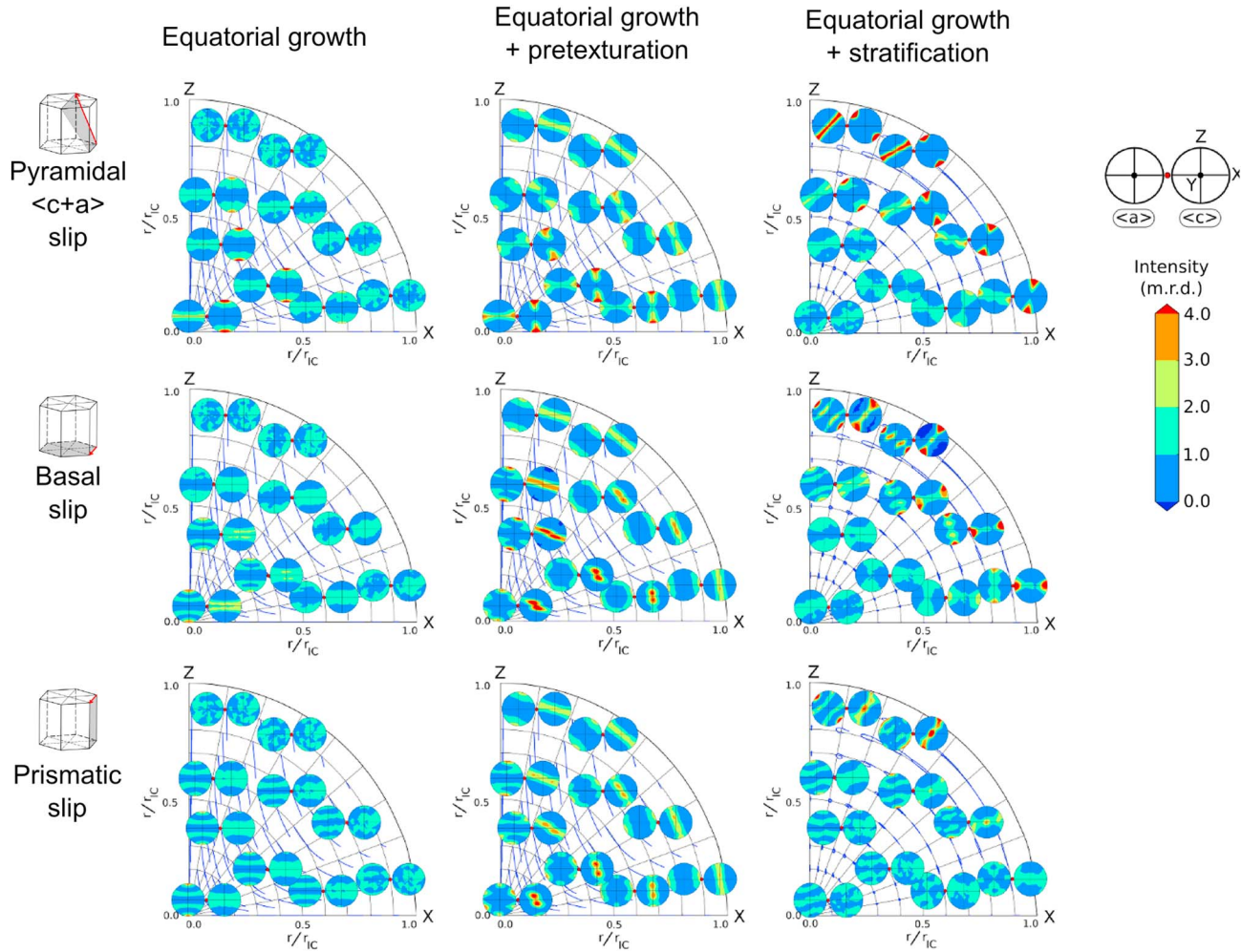
Figure 3. Pairs of pole figures of the (left column) *a* and right *c* directions representing present-day textures of the inner-core hcp alloy. Calculated with dominant pyramidal ⟨*c* + *a*⟩ slip (top row), basal slip (middle row), or prismatic slip (bottom row). Core formation models with fast crystallization at the equator (left column), with the addition of crystallization textures at the ICB (center column), or density stratification (right column). The vertical *Z* axis is the geographical South-North axis while *X* lies in the equatorial plane. Blue lines are the trajectories of the polycrystalline aggregates after crystallization at the ICB. Contours in multiples of a random distribution (m.r.d., linear scale). r_{ic} is the inner-core radius. Pyramidal slip produces the strongest global textures, with the *c* axes of the aggregate mostly aligned with the Earth's rotation axis. Simulation with other slip systems produce less consistent textures, in which the *c* axes of the aggregates can be found in multiple orientations.

2.3. Inner-Core Elasticity

Given the spread of published data for the elasticity of hcp Fe at inner-core conditions [*Vočadlo et al.*, 2009; *Sha and Cohen*, 2010; *Martorell et al.*, 2013] and the unknown influence of alloying elements, we estimate the global inner-core anisotropy as a function of single-crystal elasticity over a wide range of values. Rather than using grid points in the five-dimensional space of independent elastic constants, we generate elastic moduli by a Monte-Carlo approach.

We generate 4500 random sets of single-crystal elastic moduli which satisfy the following requirements. The Hill average of the bulk and shear moduli of the randomly oriented aggregate should be within 15% of inner-core values (K = 1400 GPa and G = 170 GPa) [*Dziewoński and Anderson*, 1981]. The single-crystal elastic moduli should also satisfy conditions for mechanical stability for hcp [*Wallace*, 1972]

$$C_{11} - C_{12} > 0;$$
$$C_{11} + C_{12} + C_{33} > 0;$$
$$(C_{11} + C_{12})C_{33} - 2\,C_{13}^2 > 0;$$
$$C_{44} > 0,$$

(1)

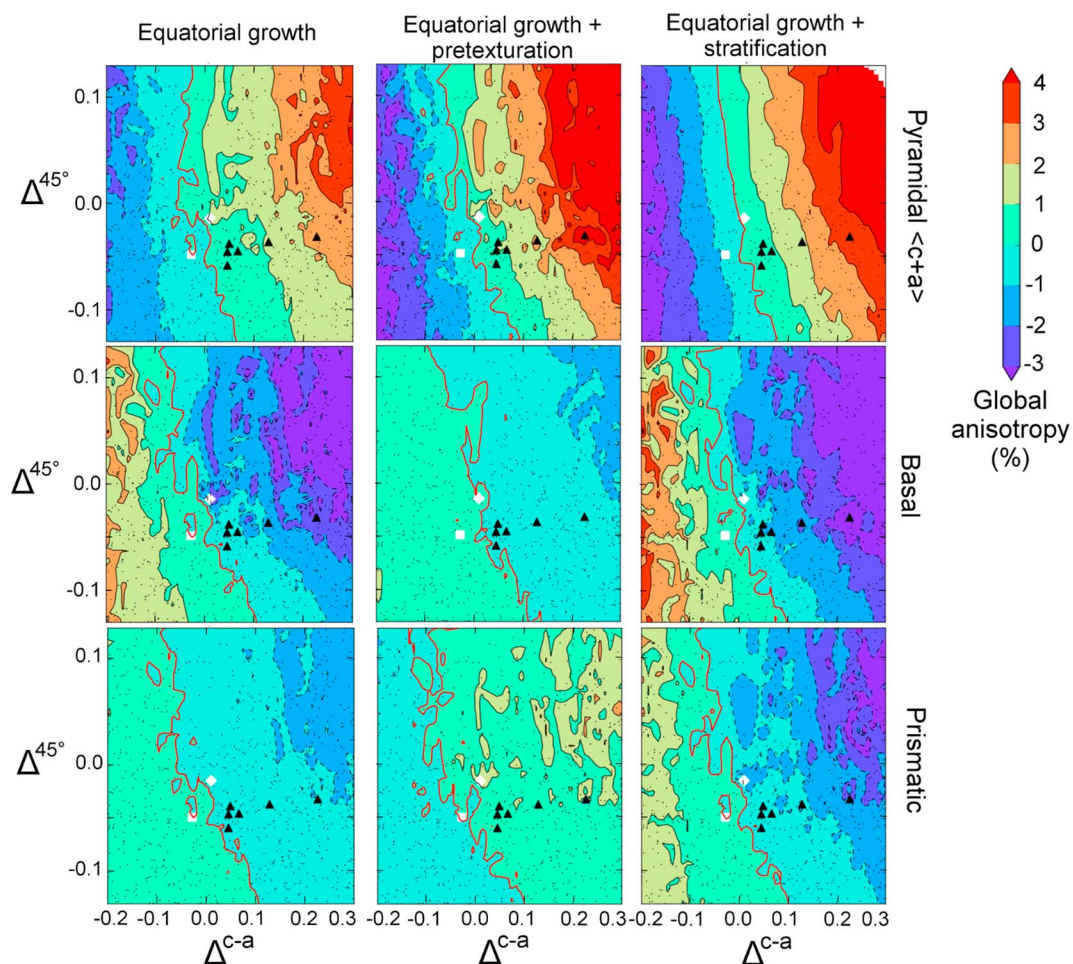where C_{ij} are single-crystal elastic moduli.

Figure 4. Global inner-core anisotropy (color scale) versus single-crystal anisotropy parameters Δ^{c-a} and $\Delta^{45°}$ for different core-formation models (columns) and dominant hcp slip systems (rows). Calculations were performed for 4500 random sets of elastic moduli (black dots) and the contour lines are obtained by interpolation. First-principles calculations for hcp Fe single-crystal elasticity at inner-core conditions are shown as white diamond for *Vočadlo et al.* [2009], white square for *Sha and Cohen* [2010], and black triangles for *Martorell et al.* [2013] that include an effect of premelting.

For each inner-core formation model, elastic model, and marker position, we calculate the polycrystalline elastic tensor using the simulated textures and single-crystal elastic moduli.

2.4. Inner-Core Seismic Anisotropy

More than 300,000 synthetic seismic rays are generated randomly to probe the whole inner core. For each ray, we estimate the normalized seismic travel times residual $\delta t/t = (s - s^0)/s^0$, where s is the simulated slowness of the seismic ray and s^0 is the slowness of that same ray for an homogeneous and fully isotropic inner core [*Lincot et al.*, 2014].

Many seismological studies use averaging procedures with travel times residuals fitted to [*Creager*, 1992; *Deuss*, 2014]

$$\delta t/t = a_1 + a_2 \cos^2 \zeta + a_3 \cos^4 \zeta, \tag{2}$$

where a_1, a_2, and a_3 are adjustable parameters and ζ is the angle between the ray and the Earth's rotation axis. The quantity $a_2 + a_3$ is the difference between polar ($\zeta = 0°$) and equatorial ($\zeta = 90°$) residuals. It is a measure of the global inner-core anisotropy often reported in the literature. It will be used in the rest of the paper (Figure 4).

3. Results

3.1. Parameters for hcp Single-Crystal Anisotropy

Despite the complexity introduced by elasticity, crystal plasticity, geodynamics, and seismic rays geometry, two dimensionless elastic parameters are found to primarily affect the global inner-core anisotropy: Δ^{c-a} and $\Delta^{45°}$. Δ^{c-a} describes the relative difference in P waves velocities along the c and a axes (V_P^c and V_P^a), and $\Delta^{45°}$ is related to the concavity of the single-crystal P wave velocities, 45° away from the c axis ($V_P^{45°}$). They are calculated as follow

$$\Delta^{c-a} = \frac{V_P^c - V_P^a}{V_P^m},$$

$$\Delta^{45°} = \frac{V_P^{45°} - \left(V_P^c + V_P^a\right)/2}{V_P^m}, \tag{3}$$

where V_P^m is the average P wave velocity.

Global anisotropy results are consistent when plotted as a function of Δ^{c-a} and $\Delta^{45°}$: they reveal parallel isocontour mainly controlled by Δ^{c-a} (Figure 4). This analysis allows to classify our 4500 sets of random elastic moduli and other calculations from the literature in a simple representation and estimate their effect on global inner-core anisotropy.

3.2. Inner-Core Anisotropy

Seismic studies report global inner core anisotropy of up to several percents with North-South velocities larger than those in the equatorial plane [*Deuss*, 2014; *Tkalčić*, 2015]. As shown in Figure 4, this level of anisotropy is difficult to reach if deformation of the inner-core hcp alloy is controlled by dominant basal or prismatic slip, irrespectively of the inner-core formation model. Indeed, inner-core anisotropy is measured with waves crossing the entire inner core. If polycrystalline textures are not consistent over large regions, the anisotropy of the single crystal will be canceled at the global scale of the seismic measurement.

Pyramidal $\langle c + a \rangle$ slip, on the other hand, is prone to align the c axes of an aggregate during its deformation. Hexagonal crystals are axisymmetric around the single-crystal c axis for elasticity. As such, this mechanism allows for significant enhancement of the global scale inner-core anisotropy. With dominant pyramidal $\langle c+a \rangle$ slip, faster velocities along single-crystal c axes ($\Delta^{c-a} > 0$) are required to obtain a positive global anisotropy. $\Delta^{45°}$ acts as a secondary but nonnegligible factor: a concave variation of the velocities ($\Delta^{45°} > 0$) tends to amplify the global anisotropy.

Models with dominant pyramidal $\langle c + a \rangle$ slip, faster crystallization in the equatorial region, and random crystallization textures at the solidification front produce global anisotropies 5 to 15 times smaller than Δ^{c-a} at the single-crystal level. The addition of solidification textures not only enhances the global anisotropy but also adds scatter in the representation of Figure 4 with a few models with $\Delta^{c-a} < 10\%$ producing a global anisotropy larger than 3%. In such model, textures produced in the central portions of the inner core are induced by plastic deformation, with a global cylindrical symmetry, whereas the outer portions of the inner core are mostly influenced by solidification textures with a global spherical symmetry (Figure 3). This induces heterogeneities in travel time calculations and scatter in the representation of Figure 4. The addition of stratification reinforces the global anisotropy by up to 50%. For example, in the stratified model with dominant pyramidal $\langle c + a \rangle$ slip, single-crystal anisotropies with Δ^{c-a} between 5 and 20% are required for a global anisotropy between 1 and 3%.

4. Discussion and Conclusion

Previous studies have shown that bcc and fcc phases orientation through dislocation creep cannot explain the observed North-South global inner-core anisotropy [*Lincot et al.*, 2015] . Here we show that an hcp inner-core Fe alloy, deforming plastically along a dominant pyramidal $\langle c+a \rangle$ slip system, with 5 to 20% elastic anisotropy in the single crystal, and a simple low-degree inner-core formation model can produce a global anisotropy of 1 to 3%.

Hexagonal crystals are axisymmetric around their c axis for elasticity. As such, a most efficient model of inner-core anisotropy should align the c axes of the hcp aggregates with the Earth's rotation axis. This ingredient is crucial for reproducing inner-core anisotropy and can be obtained if the plasticity of the inner-core hcp alloy is dominated by pyramidal $\langle c + a \rangle$ slip.

Figure 4 allows for constraining Δ^{c-a} and $\Delta^{45°}$ for single-crystal elastic tensors compatible with anisotropy observations. Do note, however, that our solution for single-crystal elasticity is not unique. First-principles calculations for stable hcp Fe at inner-core conditions [*Vočadlo et al.*, 2009; *Sha and Cohen*, 2010] lead to a weak single-crystal anisotropy and weak global anisotropy, below 1% (Figure 4). Recently, it was shown that hcp Fe may exhibit a strong nonlinear shear weakening just before melting, with a reduction in V_S and a large increase in single-crystal anisotropy [*Martorell et al.*, 2013]. With such elastic moduli, our multiscale model is successful at reproducing inner-core global seismic anisotropy (Figure 4).

A large-scale coherent alignment of anisotropic Fe alloy through the inner core is required to reproduce a North-South global seismic anisotropy, which likely requires that crystal alignment is due to a low-degree deformation field. A more complex geometry like, for example, high Rayleigh number convection could generate locally strong textures, but such anisotropy would be canceled at the scale of seismic observations.

At this point, other details of the scenario of inner-core formation cannot be discriminated. Observations of inner-core anisotropy are constrained by a distinct set of specific ray paths—a few hundreds—that are now being supplemented by the addition of virtual paths using the cross correlation of ambient noise and earthquake coda [*Wang et al.*, 2015; *Boué et al.*, 2014]. In addition, the representation of seismic observations with fits (equation (2)) oversimplifies the data by smoothing the geographical and depth dependence of the seismic travel times. In the future, such direct multiscale model should be extended for inverting the actual observations of seismic travel times, including their radial and lateral variations [*Deuss*, 2014; *Tkalčić*, 2015; *Wang et al.*, 2015]. This new approach will constrain the different scenarios regarding the history of the Earth's inner core and its interactions with the outer core [*Deguen*, 2012] and the geodynamo [*Aubert et al.*, 2008].

References

Aubert, J., H. Amit, G. Hulot, and P. Olson (2008), Thermochemical flows couple the Earth's inner core growth to mantle heterogeneity, *Nature*, *454*, 758–761, doi:10.1038/nature07109.

Bergman, M. I. (1997), Measurements of elastic anisotropy due to solidification texturing and the implication for the Earth's inner core, *Nature*, *389*, 60–63, doi:10.1038/37962.

Boué, P., P. Poli, M. Campillo, and P. Roux (2014), Reverberations, coda waves and ambient noise: Correlations at the global scale and retrieval of the deep phases, *Earth Planet. Sci. Lett.*, *391*, 137–145, doi:10.1016/j.epsl.2014.01.047.

Brito, D., D. Elbert, and P. Olson (2002), Experimental crystallization of gallium: Ultrasonic measurements of elastic anisotropy and implications for the inner core, *Phys. Earth Planet. Int.*, *129*, 325–346, doi:10.1016/S0031-9201(01)00298-9.

Buffett, B. A. (2009), Onset and orientation of convection in the inner core, *Geophys. J. Int.*, *179*, 711–719, doi:10.1111/j.1365-246X.2009.04311.x.

Buffett, B. A., and H.-R. Wenk (2001), Texturing of the Earth's inner core by Maxwell stresses, *Nature*, *413*, 60–63, doi:10.1038/35092543.

Creager, K. C. (1992), Anisotropy of the inner core from differential travel times of the phases PKP and PKIKP, *Nature*, *356*, 309–314, doi:10.1038/356309a0.

Deguen, R. (2012), Structure and dynamics of Earth's inner core, *Earth Planet. Sci. Lett.*, *333-334*, 211–225, doi:10.1016/j.epsl.2012.04.038.

Deguen, R., and P. Cardin (2009), Tectonic history of the Earth's inner core preserved in its seismic structure, *Nat. Geosci.*, *2*, 419–422, doi:10.1038/ngeo522.

Deguen, R., S. Merkel, R. A. Lebensohn, and P. Cardin (2011), Texturing in Earth's inner core due to preferential growth in its equatorial belt, *Phys. Earth Planet. Inter.*, *188*, 173–184, doi:10.1016/j.pepi.2011.08.008.

Deuss, A. (2014), Heterogeneity and anisotropy of Earth's inner core, *Ann. Rev. Earth Planet. Sci.*, *42*, 103–126, doi:10.1146/annurev-earth-060313-054658.

Deuss, A., J. C. E. Irving, and J. H. Woodhouse (2010), Regional variation of inner core anisotropy from seismic normal mode observations, *Science*, *328*(5981), 1018–1020, doi:10.1126/science.1188596.

Dziewoński, A. M., and D. L. Anderson (1981), Preliminary reference Earth model, *Phys. Earth Planet. Inter.*, *25*, 297–356, doi:10.1016/0031-9201(81)90046-7.

Gubbins, D., D. Alfè, and C. J. Davies (2013), Compositional instability of Earth's solid inner core, *Geophys Res. Lett.*, *40*, 1084–1088, doi:10.1002/grl.50186.

Karato, S. (1999), Seismic anisotropy of the Earth's inner core resulting from flow induced Maxwell stresses, *Nature*, *402*, 871–873, doi:10.1038/47235.

Lasbleis, M., R. Deguen, P. Cardin, and S. Labrosse (2015), Earth's inner core dynamics induced by the Lorentz force, *Geophys. J. Int.*, *202*, 548–563, doi:10.1093/gji/ggv155.

Lebensohn, R. A., and C. N. Tomé (1993), A selfconsistent anisotropic approach for the simulation of plastic deformation and texture development of polycrystals: Application to zirconium alloys, *Acta Metall. Mater.*, *41*, 2611–2624, doi:10.1016/0956-7151(93)90130-K.

Lincot, A., R. Deguen, S. Merkel, and P. Cardin (2014), Seismic response and anisotropy of a model hcp iron inner core, *C. R. Geosci.*, *346*, 148–157, doi:10.1016/j.crte.2014.04.001.

Lincot, A., S. Merkel, and P. Cardin (2015), Is inner core seismic anisotropy a marker of plastic flow of cubic iron?, *Geophys. Res. Lett.*, *42*, 1326–1333, doi:10.1002/2014GL062862.

Martorell, B., L. Vočadlo, J. Brodholt, and I. G. Wood (2013), Strong premelting effect in the elastic properties of hcp-Fe under inner-core conditions, *Science*, *342*, 466–468, doi:10.1126/science.1243651.

Merkel, S., H.-R. Wenk, P. Gillet, H. K. Mao, and R. J. Hemley (2004), Deformation of polycrystalline iron up to 30 GPa and 1000 K, *Phys. Earth Planet. Inter.*, *145*, 239–251, doi:10.1016/j.pepi.2004.04.001.

Merkel, S., M. Gruson, Y. Wang, N. Nishiyama, and C. N. Tomé (2012), Texture and elastic strains in hcp-iron plastically deformed up to 17.5 GPa and 600 K: Experiment and model, *Model. Simul. Mater. Sci. Eng.*, *20*, 24005, doi:10.1088/0965-0393/20/2/024005.

Miyagi, L., M. Kunz, J. Knight, J. Nasiatka, M. Voltolini, and H.-R. Wenk (2008), In situ phase transformation and deformation of iron at high pressure and temperature, *J. Appl. Phys.*, *104*, 103510, doi:10.1063/1.3008035.

Morelli, A., A. M. Dziewoński, and J. H. Woodhouse (1986), Anisotropy of the inner core inferred from PKIKP travel times, *Geophys. Res. Lett.*, *13*, 1545–1548, doi:10.1029/GL013i013p01545.

Poirier, J. P., and F. Langenhorst (2002), TEM study of an analogue of the Earth's inner core ϵ-Fe, *Phys. Earth Planet. Inter.*, *129*, 347–358, doi:10.1016/S0031-9201(01)00300-4.

Poupinet, G., R. Pillet, and A. Souriau (1983), Possible heterogeneity of the Earth's inner core deduced from PKIKP travel times, *Nature*, *305*, 204–206, doi:10.1038/305204a0.

Sha, X., and R. E. Cohen (2010), Elastic isotropy of ϵ-Fe under Earth's core conditions, *Geophys. Res. Lett.*, *37*, L10302, doi:10.1029/2009GL042224.

Singh, S. C., M. A. J. Taylor, and J. P. Montagner (2000), On the presence of liquid in the Earth's inner core, *Science*, *287*, 2471–2474, doi:10.1126/science.287.5462.2471.

Tkalčić, H. (2015), Complex inner core of the Earth: The last frontier of global seismology, *Rev. Geophys.*, *53*, 59–94, doi:10.1002/2014RG000469.

Vočadlo, L., D. P. Dobson, and I. G. Wood (2009), Ab initio calculations of the elasticity of hcp-Fe as a function of temperature at inner-core pressure, *Earth Planet. Sci. Lett.*, *288*, 534–538, doi:10.1016/j.epsl.2009.10.015.

Wallace, D. C. (1972), *Thermodynamics of Crystals*, Wiley, New York.

Wang, T., X. Song, and H. H. Xia (2015), Equatorial anisotropy in the inner part of Earth's inner core from autocorrelation of earthquake coda, *Nat. Geosci.*, *8*, 224–227, doi:10.1038/ngeo2354.

Waszek, L., J. Irving, and A. Deuss (2011), Reconciling the hemispherical structure of Earth's inner core with its super-rotation, *Nat. Geosci.*, *4*, 264–267, doi:10.1038/ngeo1083.

Wenk, H.-R., J. R. Bamgardner, R. A. Lebensohn, and C. N. Tomé (2000a), A convection model to explain the anisotropy of the inner core, *J. Geophys. Res.*, *105*, 5663–5677, doi:10.1029/1999JB900346.

Wenk, H.-R., S. Matthies, R. J. Hemley, H. K. Mao, and J. Shu (2000b), The plastic deformation of iron at pressures of the Earth's inner core, *Nature*, *405*, 1044–1047, doi:10.1038/35016558.

Woodhouse, J. H., D. Giardini, and X. D. Li (1986), Evidence for inner core anisotropy from free oscillations, *Geophys. Res. Lett.*, *13*, 1549–1552, doi:10.1029/GL013i013p01549.

Yoshida, S., I. Sumita, and M. Kumazawa (1996), Growth model of the inner core coupled with outer core dynamics and the resultant elastic anisotropy, *J. Geophys. Res.*, *101*, 28,085–28,103, doi:10.1029/96JB02700.

Zhang, P., R. E. Cohen, and K. Haule (2015), Effects of electron correlations on transport properties of iron at Earth's core conditions, *Nature*, *517*, 605–607, doi:10.1038/nature14090.